Preparation and characterization of supported $Ru_xIr_{(1-x)}O_2$ nano-oxides using a modified polyol synthesis assisted by microwave activation for energy storage applications

Thomas Audichon [a,*], Benoit Guenot [a,b], Steve Baranton [a], Marc Cretin [b], Claude Lamy [b], Christophe Coutanceau [a,*]

[a] Université de Poitiers, IC2MP, UMR CNRS 7285, "Catalysis and Non-conventional Media" Group, 4 Rue Michel Brunet, TSA 51106, 86073 Poitiers cedex 9, France
[b] Université de Montpellier, Institut Européen des Membranes, UMR ENSCM, UM, CNRS n°5635, 2 Place Eugène Bataillon, CC047, 34095 Montpellier Cedex 5, France

ARTICLE INFO

ABSTRACT

A simple and soft synthesis method, namely the polyol route, is proposed to synthesize $Ru_xIr_{(1-x)}O_2$ mixed-oxide nanoparticles deposited on a high surface area carbon support, with controlled size and size distribution, and composition. The samples are characterized by TGA, XRD, TEM, XPS and Raman analyses. Their behaviors as supercapacitors and catalysts for oxygen evolution reaction (OER) have been investigated in 0.5 M H_2SO_4 medium. It was demonstrated that pure RuO_2 presented the highest super-capacitive property, and that addition of iridium leads to decrease this property. On the other hand, pure RuO_2 presented the lower onset potential for OER, but tended to be passivated as the potential was increased. Addition of iridium led to limit or to avoid the catalyst passivation and to increase the activity at high potential, but also to shift positively the OER onset potential.

© 2016 Elsevier B.V. All rights reserved.

1. Introduction

Our technological civilization needs more and more energy, particularly in emerging and developing countries. Fossil resources, such as coal, natural gas and hydrocarbons are the main primary sources, but their amount is limited and will be exhausted in a few decades. Furthermore they are the main contribution to carbon dioxide emission leading to greenhouse effect. To overcome these energetic and environmental issues, renewable primary energy sources, such as hydroelectric, wind, solar and tidal powers, have known very intense developments for the last decades. But, most of these energy sources are intermittent and thus energy storage solutions have to be developed in parallel, either under chemical or electrochemical forms. The use of supercapacitors is a good means for electricity storage whereas hydrogen is considered as the most effective candidate for chemical storage of the energy, particularly for its further use in a polymer electrolyte membrane fuel cell. Currently, 4% of hydrogen is produced by water electrolysis and 95% by steam reforming of fossil fuels [1,2], which is not sustainable. Water electrolysis using renewable primary energy sources is a sustainable process but it still remains an expensive method for producing high-purity hydrogen. The reason is the high anode overpotential for the oxygen evolution reaction (OER), which leads to high cell voltage, i.e. high energy consumption [3].

Among the many transition metal oxides, the most success has been achieved using RuO_2 for supercapacitors due to its advantages of a wide potential window, of highly reversible redox reactions, long life cycle and metallic type conductivity [4]. Indeed, RuO_2 has a well-known application as Dimensionally Stable Anode in energy storage electrochemical supercapacitors [5]. RuO_2, which exhibits low resistivity, metallic conductivity, and high thermal and chemical stabilities, is also a basic material as a corrosion-resistant electrode at low overpotentials for chlorine and oxygen evolution reactions [6,7]. The overpotential of OER in acid medium is indeed comparatively lower when RuO_2 is used as catalyst than in the case of other metals or oxides. However, in order to increase its stability and activity towards the OER, ruthenium oxide is often mixed with iridium oxide [6]. Indeed, due to their high electrochemical performances, ruthenium oxide (RuO_2) and iridium oxide (IrO_2) have been extensively investigated as anodes for O_2 evolution in acidic medium [8,9].

Fundamental investigations and extensive researches on synthesis methods for the production of RuO_2 based catalysts have

been performed in order to obtain the material structure and composition fulfilling the compromise between property requirements of the considered application and cost. The rutile-type RuO_2 surface properties as well as its electrochemical behavior (electrocatalytic activity, selectivity, stability) are indeed known to depend on the precursor materials, preparation conditions and pyrolysis treatment [10]. In a previous work, we reported a simple and rapid method (the microwave assisted "Instant method") for the synthesis of RuO_2 and the way to tune the structure/property of the rutile-type material, for either water electrolysis reaction or capacitor application [11].

The present study is devoted to a simple, effective and economic synthesis route for a large scale synthesis of RuO_2 and IrO_2 nanoparticles, which respects the following principles: time, energy and atom savings, non-harmful chemical synthesis, safe and environmental-friendly synthesis process. The soft microwave activated polyol route under oxygen atmosphere adopted in this work for synthesizing $Ru_xIr_{1-x}O_2$ mixed oxides leads to the formation of pure and nanosized compounds. The purpose of this work is to use a simple and clean synthesis procedure with special attention paid to the characterization of the obtained $Ru_xIr_{1-x}O_2$ particles in terms of microstructures, electrocatalytic behavior towards OER in acidic solution and capacitive properties. For this purpose, in order to decrease the metal loading in the electrode and to be able to characterize the own behavior of $Ru_xIr_{1-x}O_2$ mixed oxides at the nanoparticle level, the materials were dispersed on an inactive high surface area electron-conducting carbon powder.

2. Experimental

2.1. Mixed oxides synthesis

Mixed oxides supported on a carbon powder (Vulcan XC 72) were synthesized by a modified polyol method. Appropriate amounts of $H_2IrCl_6 \cdot 6H_2O$ and/or $RuCl_3 \cdot 3H_2O$, (99.9% purity, Alfa Aesar) were dissolved in 50 mL of ethylene glycol (puriss. p.a., purity ≥99.5%, Fluka) with nominal metal concentrations corresponding to Ru:Ir atomic ratios of 1:0, 0.75:0.25, 0.5:0.5, 0.25:0.75 and 0:1 in order to obtain a final oxide concentration of 1 g L^{-1}. A NaOH solution (1 M) in ethylene glycol was then added drop-wise in the mixture under N_2 bubbling (Nitrogen U quality from "Air Liquide") to adjust the pH to 11. The reactor was equipped with a cooler and placed in a microwave oven MARS 5 (CEM Corporation). The mixture temperature was increased up to 180 °C in less than 2 min (microwave power of 1600 W) and kept at this temperature for 20 min. In order to obtain directly metal oxide nanoparticles, all the procedure was realized under O_2 bubbling. After solution has cooled down to room temperature, 200 mg of carbon Vulcan XC72 (preliminary thermally treated for 4 h at 400 °C under U Quality Nitrogen) was added to obtain a nominal metal oxide loading of 20 wt% on carbon. To obtain a better dispersion of particles on the substrate, the mixture was ultrasonically homogenized for 1 h. Then, 50 mL of ultra-pure water (MilliQ, Millipore, 18.2 MΩ cm) was added and the pH was decreased to 1 by drop-wise addition of a HNO_3 solution (70% Sigma Aldrich). The resulting suspension was filtrated and washed with ultra-pure water. The catalytic powder was finally dried at 80 °C overnight.

2.2. Electrochemical measurements

Electrochemical measurements were carried out in a standard three-electrode electrochemical cell at 20 °C. A reversible hydrogen electrode (RHE) and a glassy carbon slab were used as reference and counter electrodes, respectively. The RHE was connected to the cell via a Luggin capillary. The 0.5 mol L^{-1} H_2SO_4 (Merck, Supra-

pur) aqueous electrolyte was prepared with ultrapure water. A gold plate of 0.4 cm^2 geometric surface area was used as the working electrode. Before each experiment, the electrolyte was purged by bubbling nitrogen (U quality) for 15 min and the nitrogen atmosphere was maintained in the electrochemical cell during the experiment. Then, in order to check the cleanliness of the gold support and of the cell, cyclic voltammograms were recorded in the supporting electrolyte prior to catalytic metal deposition. The potential-current density curves were recorded using a Model 362 Scanning Potentiostat from Princeton Applied Research connected to a computer. Catalytic inks were prepared by mixing a suspension consisting of 10.8 mg of the supported metal oxides in 3 mL of ultrapure water. For each electrochemical experiment, the anode was prepared by depositing 11.4 μL of the catalytic ink onto each face of the gold plate, which corresponded to a total of 0.2 mg of catalyst per cm². The ink was first dried under a slow nitrogen flow (U quality) and then 4 μL of a Nafion solution consisting in Nafion (5 wt% in aliphatic alcohol from Aldrich) dispersed in ultrapure water with a mass concentration of $2 \text{ g}_{\text{Nafion}} \text{ L}^{-1}$, was deposited on the catalyst layer, corresponding to a loading 20 wt% of Nafion with respect to the carbon supported catalyst mass.

2.3. Physical and physicochemical characterizations

The morphology of the materials was examined by transmission electron microscopy (TEM). TEM images were acquired with a JEOL 2100UHR (200 kV) electron microscope equipped with a LaB_6 filament. TEM grids were prepared by depositing a drop of a suspension of metal oxide/C in ethanol on a copper grid and by evaporating the solution in the open atmosphere. The mean particle sizes and size distributions were determined using ImageJ free software. Thermogravimetric analyses (TGA) were performed with a TA Instruments SDT Q600 apparatus. The measurements were done by heating ca. 5 mg of the catalytic powder in an alumina crucible under air flow (100 mL min⁻¹) from 25 to 900 °C with a heating rate of 5 °C min⁻¹. Raman spectra were recorded using a Raman confocal microscope HORIBA JOBIN YVON HR800 UV equipped with an internal Ar laser emitting at a wavelength of 514.5 nm and a CCD detector. The laser powers for the analysis varied from 0.04 to 4.00 mW. The surface compositions of metal oxide materials were evaluated through X-ray photoelectron spectroscopy (XPS) measurements. Analyses were carried out with a Kratos Axis Ultra DLD spectrometer equipped with a monochromatic Al Kα source (1486.6 eV) operating at 150 W (10 mA, 15 kV). The instrument base pressure was 9×10^{-8} Pa. The catalytic powder was pressed in a copper holder of 3 mm diameter and introduced into the preparation chamber. After being outgassed overnight, high-resolution spectra were recorded with 20 eV pass energy on an analysis area of 300 μm × 700 μm. These experimental parameters corresponded to Ag $3d_{5/2}$ FWHM (full width at half maximum) of 0.55 eV. Data were acquired with 0.1 eV steps. The binding energy was calibrated with that of C 1 s fixed at 284.4 eV as an internal reference. Spectra were fitted with CasaXPS software (version 2.3.17). Shirley background has been chosen, and Ru 3d and Ir 4f peak fittings were performed using asymmetric Gaussian−Lorentzian profile functions.

3. Results and discussions

3.1. Physicochemical characterizations

TEM measurements were undertaken to analyse the morphologies, the dispersions and the particle sizes of metal oxide materials deposited on the carbon substrate. TEM images of the $Ru_xIr_{(1-x)}O_2/C$ catalysts synthesized by the modified polyol method are depicted
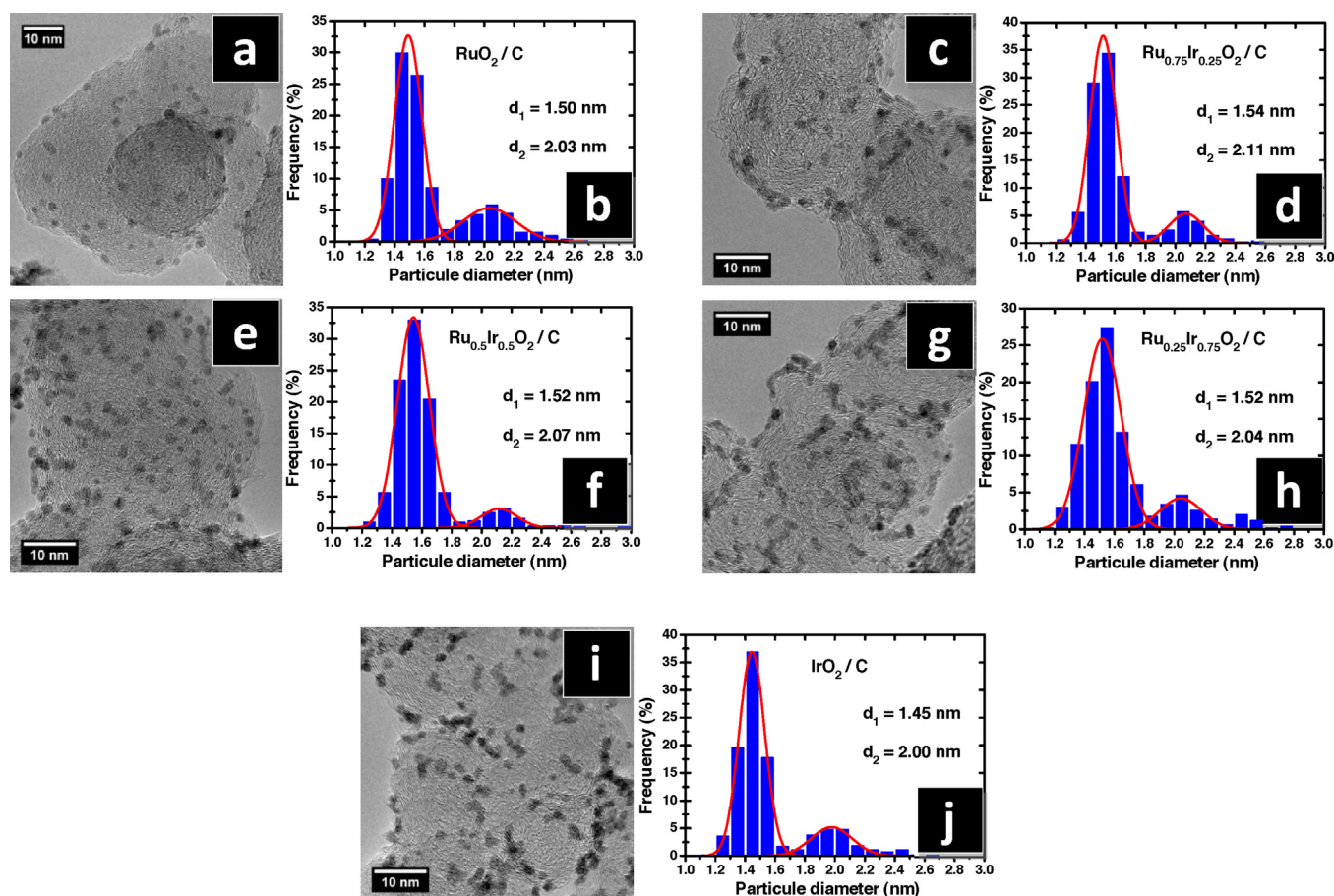
Fig. 1. Typical transmission electron microscopy (TEM) image and corresponding particles size distribution for RuO_2/C (a-b); $Ru_{0.75}Ir_{0.25}O_2/C$ (c-d); $Ru_{0.5}Ir_{0.5}O_2/C$ (e-f); $Ru_{0.25}Ir_{0.75}O_2/C$ (g-h) and IrO_2/C (i-j) materials.

in Fig. 1a,c,e,g,i. All samples present well-defined uniform spherical particles, which are highly dispersed on the carbon substrates. The presence of two metals in mixed metal oxides does not affect significantly the morphology and the geometric structure of the particles. At low magnification, few regions with aggregated particles could be seen, but no evidence of aggregation level change with the sample composition was observed. From TEM images, the mean particles size for each sample was determined by measuring the diameter of 500 isolated particles. The histograms are presented in Fig. 1b,d,f,h,j and a bimodal particle size distribution appears for all samples. For all $Ru_xIr_{(1-x)}O_2/C$ materials, ca. 80% of particles have a mean diameters of ca. 1.5 nm, and ca. 20% of ca. 2.0 nm. Conversely to carbon nanotube support [12], the deposition of metal oxide on the carbon powder support prevents particle sintering and growth processes and leads to size controlled nanoparticles.

Thermogravimetric analyses were carried out in order to determine the weight loadings of metal oxides on the carbon substrate and to compare these values with the nominal ones (20 wt% for each material synthesized). The TGA and DTA curves obtained for $Ru_xIr_{(1-x)}O_2/C$ catalysts are given in Fig. 2. Four distinct temperature regions are present for all metal oxide compositions. The first region between 25 °C and 175 °C is characterized by a low weight loss, between 1% for pure iridium oxide and 3% for pure ruthenium oxide. Although, no distinguishable endothermic peaks are present on the DTA curves, the mass decrease could be attributed to desorption of physically adsorbed impurities and/or water from the surface of the carbon supported catalysts. In the range from 175 °C to 300 °C, a second weight loss occurs which can be attributed to desorption of chemically bounded water molecules, as often described in the
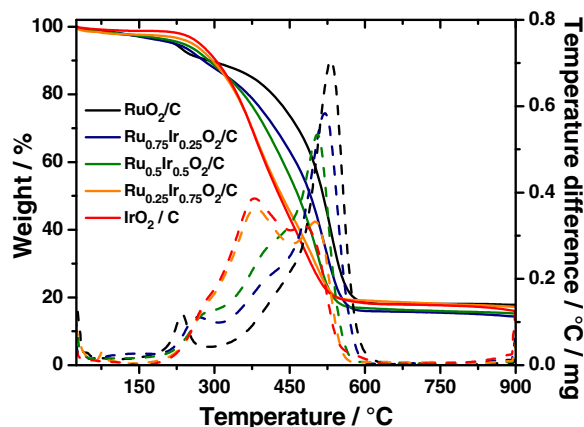

Fig. 2. Thermo-gravimetric analysis (TGA) and thermo-differential analysis (DTA) of $Ru_xIr_{(1-x)}O_2/C$ catalysts ($\Delta T = 5 °C\,min^{-1}$; air flow $100\,mL\,min^{-1}$).

literature [11,12]. The low decrease of weight is accompanied by a clearly defined exothermic peak at 235 °C on the DTA curves for RuO_2/C. When increasing the iridium oxide ratio, the position of the DTA peak shifts towards higher temperatures becoming only a shoulder at ca. 277 °C for $Ru_{0.25}Ir_{0.75}O_2$ and IrO_2. Then, in the range from 300 to 600 °C, the combustion of carbon support takes place, leading to weight loss of approximately 80% for each sample. The broad exothermic peak at 530 °C on the DTA curves of RuO_2/C material is assigned to the carbon loss. When increasing the iridium molar composition in the supported oxide particles, the tempera-
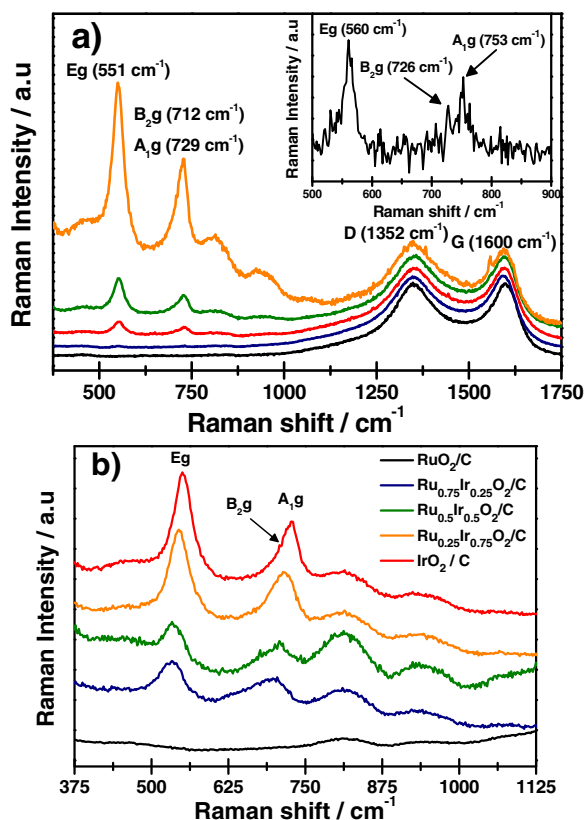
Fig. 3. (a) Raman spectra of IrO_2/C material at different laser power: 0.04 (black line); 0.4 (blue line); 1 (red line); 2 (green line) and 4 mW (orange line). Inset: spectra obtained at 0.04 mW after power evolution measurement. (b) Raman spectra of $Ru_xIr_{(1-x)}O_2$/C catalysts obtained at 4 mW (For interpretation of the references to colour in this figure legend, the reader is referred to the web version of this article.)

ture of the exothermic peak decreases and a splitting in two peaks at 380 and 480 °C occurs for IrO_2 and $Ru_{0.25}Ir_{0.75}O_2$. The temperature change of the carbon support degradation indicates that the presence of iridium oxide catalyzes the carbon combustion giving an ATD peak at lower temperatures. Finally, for temperatures greater than 600 °C, the sample weights remain constant.

The final weight percentages are attributed to the remaining oxide particles. Results obtained after correction of physically adsorbed impurities and/or water contributions are summarized in Table 1. The values are close to the nominal ones, and the differences could come from standard deviations of measurements and/or experimental synthesis uncertainties. Moreover, considering that oxygen represents 24.0% and 14.2% of the total mass of the pure ruthenium and iridium oxides, respectively, weight percentage values of 15.2% and 17.1% would be expected if Ru and Ir metallic particles were formed, respectively. The values obtained by TGA measurements are higher, which tends to confirm the oxide nature of the particles, at least of their surfaces.

Raman spectroscopy was used to identify the nature of the materials synthesized. Fig. 3a presents the Raman spectra obtained for IrO_2/C samples under different laser powers from 0.04 to 4 mW. At low laser power the spectra present only the D and G bands of the carbon structure located at 1352 and 1600 cm^{-1} [13], respectively. This observation is in accordance with results obtained for oxides deposited on carbon support without heat treatment [14]. When increasing the laser power, Raman spectrum shows two major Raman features, at 551 and 729 cm^{-1}, which look like those of crystalline IrO_2/CNTs/graphene obtained by Shih et al. [15]. Furthermore, a shoulder appears on the second peaks at 712 cm^{-1}. Liao et al. [16] established that an IrO_2 single crystal

of rutile type displays spectrum with three characteristic bands at 561 cm^{-1}, 728 cm^{-1} and 752 cm^{-1}, corresponding to Eg, A_1g and B_2g modes, respectively. Based on these results, the three contributions observed here are attributed to the Eg, A_1g and B_2g modes and the red-shift could originate from a particle size effect [15,17]. Moreover, after measurements with increased laser powers, the spectrum recorded at 0.04 mW (Fig. 3a Inset) reveals three peaks located at wavenumber values closer to the characteristic ones. The effect of high laser power on the crystalline structure is similar to a heat treatment, which allows detecting the characteristic bands of the rutile lattice of iridium oxide. Two others broad peaks appearing at 820 and 950 cm^{-1} with increasing laser power are not attributed; they could be linked to species formed after carbon combustion induced by laser irradiation, since their presences are observed on all spectra (Fig. 3b) independently on the particle nature.

Fig. 3b shows the obtained results for all $Ru_xIr_{(1-x)}O_2$/C samples with a 4 mW laser power. The spectrum of RuO_2/C sample displays no defined bands [14,18,19], which is observed for all laser power settings (not shown). Raman analyses do not allow defining the nature and the structure of the RuO_2/C material. Conversely, all materials containing iridium oxide present in their Raman spectra the three characteristic Eg, A_1g and B_2g bands of the rutile structure. These bands undergo a red shift when increasing the ratio of ruthenium oxide in the material which could be attributed to the rutile structure of ruthenium oxide with characteristic bands at 528 cm^{-1}, 646 cm^{-1} and 716 cm^{-1} for Eg, A_1g and B_2g modes [20,21]. The gradual red shift of the E_g band and the fact that no splitting occurs for the A_{1g} and B_{2g} bands may indicate a lattice modification and the formation of mixed metal oxide particles with substitution of Ir atoms in the rutile structure by Ru atoms.

XPS analysis were carried out to determine the nature of the particles and the atomic metal surface composition of the $Ru_xIr_{(1-x)}O_2$/C materials. The Ru 3d and O 1s as well as the Ir 4f and O 1s core level spectra of RuO_2/C and IrO_2/C materials are displayed in Fig. 4. The spectrum in Fig. 4a shows the important contribution of the carbon support (C 1s at 284.4 eV), and the asymmetric peak of Ru at 281.3 eV which is characteristic of the Ru 3d core level [22]. The XPS spectrum for IrO_2/C (Fig. 4c) reveals characteristic shapes of Ir 4f core level [23]. For both pure oxide materials, the shapes of the O 1s core level spectra (Fig. 4b and d) are similar. Only one broad core level peak is observed at 530.6 and 531.2 eV for RuO_2/C and IrO_2/C, respectively. The contribution of the C 1s was determined on pure Vulcan XC-72 powder, which serves as support for oxide materials, and was used for the Ru 3d core level spectrum fitting. Based on the literature [24], the Ru 3d XPS spectrum for RuO_2/C was fitted with two primary spin-orbit components at 281.1 and 285.3 eV for Ru $3d_{5/2}$ and Ru $3d_{3/2}$, respectively. In addition to the dominant spin-orbit doublets, two satellite peaks at 282.8 and 287.0 eV are attributed to final-state screening effects (green curves, Fig. 4a), which was explained by Näslund et al. as being "derived from the strong Coulomb interaction between valence electrons and the core hole produced in the photoionization process" [24]. For Ir 4f core level, the peaks located at 61.6 and 64.6 eV are attributed to the +IV oxidation number of the iridium and correspond to the $4f_{7/2}$ and $4f_{5/2}$ contributions, respectively. At energies 2.0 eV higher than that of the spin-orbit doublets, two others broad peaks are observed and attributed to the satellites peaks induced by the final-state screening effects. For both pure oxide materials, the O 1s core level signals show four components. The first ones at lower binding energies, 529.9 and 530.5 eV for RuO_2/C and IrO_2/C, respectively, are attributed to oxygen bonded to the metal (O^{2-}) and are directly correlated to the dominant spin-orbit doublets of Ru 3d and Ir 4f. The second components at 531.1 and 531.7 eV for RuO_2/C and IrO_2/C, respectively, can also be attributed to O^{2-}, but linked to the satellite peaks of the metallic species and induced by screening effects. However, these

Table 1
Physicochemical parameters obtained for $Ru_xIr_{(1-x)}O_2/C$ materials synthesized by modified polyol synthesis.

	wt % from TGA	% Atom from XPS					
		Ru 3d	Ir 4f	O 1s	C 1s	O 1s/(Ru 3d + Ir 4f)	Ru 3d/Ir 4f
RuO_2/C	20.2	3.1	–	7.8	86.6	2.5	–
$Ru_{0.75}Ir_{0.25}O_2/C$	17.0	1.3	0.5	5.6	86.7	3.1	2.6
$Ru_{0.5}Ir_{0.5}O_2/C$	17.9	1.1	1.5	7.9	86.7	3.0	0.7
$Ru_{0.25}Ir_{0.75}O_2/C$	19.4	0.7	2.4	5.7	87.5	1.7	0.3
IrO_2/C	17.5	–	3.3	6.3	88.5	1.9	–
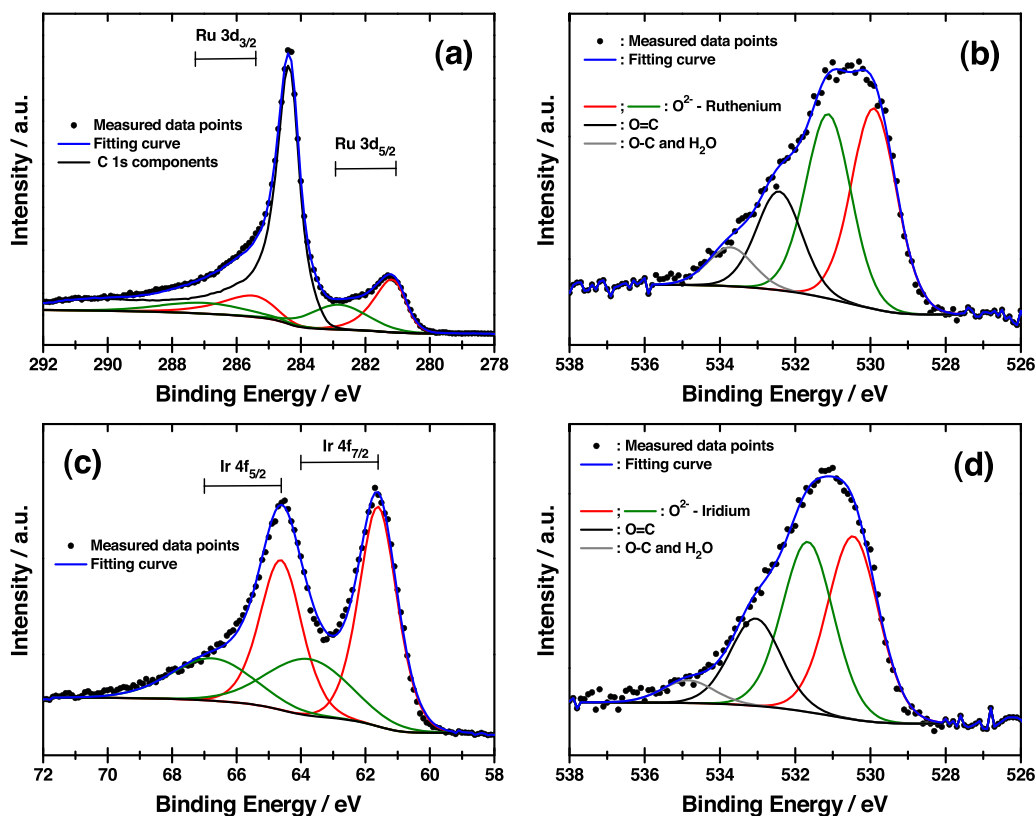
Fig. 4. XPS spectra of (a) the Ru 3d and (b) O 1s for RuO_2/C material, and (c) Ir 4f and (d) O 1s for IrO_2/C material, fitted with Gaussian-Lorentzian curves on Shirley backgrounds.

components could also be induced by a contribution of hydroxyl groups present on the oxide particles surface [25]. At last, the third and fourth components are linked to the oxygen bonded to the carbon support and are attributed to –C—O and —C═O, respectively. The same fitting procedure of XPS results was applied for the mixed metal oxides supported on Vulcan XC-72, allowing determining the atomic ratios of each element present in the oxide materials. The obtained values are summarized in Table 1. For high Ir concentration in metal oxides, the ratios O1s/(Ru 3d + Ir 4f) indicate a stoichiometry close to 2 in agreement with that expected for pure dioxide material, while for ruthenium rich material, the stoichiometry is higher than 2. This could come from a more consequent presence of hydroxyl species in Ru oxide materials [22], which tends to demonstrate that the formation of hydroxyl groups occurs preferentially on the ruthenium oxide particles. The Ru 3d/Ir 4f surface atomic ratios were determined for the mixed oxide materials. The obtained results are in accordance with the nominal values, but it seems that a very slight iridium surface enrichment takes place.

3.2. Electrochemical characterizations

Cyclic voltammograms were recorded at $20\,mV\,s^{-1}$ to determine the nature of the particles synthesized and to characterize their behaviour in H_2SO_4 supporting electrolyte in the potential range from 0.05 to 1.4 V vs. RHE (Fig. 5). All currents were normalized to the geometric surface area of the working electrode. The voltammogram shapes of the pure oxides are characteristic of ruthenium and iridium oxides supported on carbon, respectively [26]. The CV of RuO_2/C obtained is characteristic of amorphous or hydrated RuO_2 [27], which is in accordance with TGA and Raman analyses. The broad reversible peaks at 0.6 V vs. RHE are attributed to the Ru(III)/Ru(IV) redox couple, whereas the small shoulders at 0.8 V and 1.15 V vs RHE correspond to the redox transitions Ru(IV)/Ru(VI) and Ru (VI)/Ru(VIII), respectively [28]. On the other hand, the cathodic peak often described in the literature for potentials lower than 0.3 V [29,30] is not present in the case of RuO_2/C material prepared by the modified polyol synthesis method. This non-reversible peak was attributed to the insertion or absorption of hydrogen in the oxide lattice and directly linked to the sample
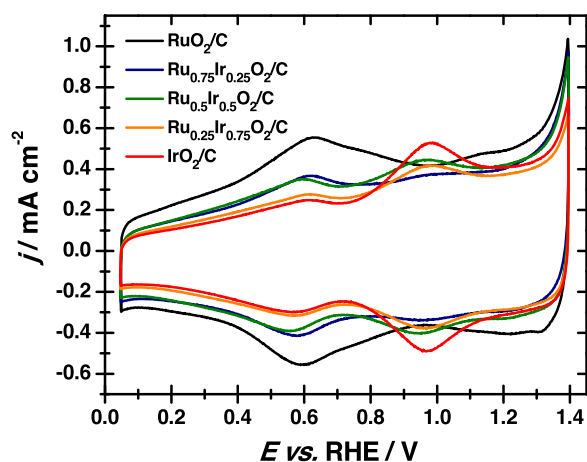
Fig. 5. Cyclic voltammograms of $Ru_xIr_{(1-x)}O_2/C$ catalysts based electrodes in 0.5 mol L^{-1} H_2SO_4 electrolyte recorded at 20 mVs^{-1} and ambient temperature.

crystallinity [31]. In the present case, the mean Ru oxide particle size of ca. 1.5 nm determined by TEM induces a low crystallite size avoiding this insertion reaction to take place. For IrO_2/C, the CV is different; two well-defined peaks are distinguishable. By analogy, the peaks at 0.6 and 1.0 V vs. RHE are reasonably attributed to the Ir(III)/Ir(IV) and Ir(IV)/Ir(VI) redox transitions, respectively [28]. For mixed ruthenium-iridium oxide catalysts, the voltammogram shapes are close to that obtained for IrO_2/C, although overlap of both Ir and Ru redox processes occurs. When decreasing the iridium content in catalysts, the current densities attributed to the Ir(IV)/Ir(VI) redox transition decrease whereas those for Ru(III)/Ru(IV) increase and a slight potential shift is observed.

Cyclic voltammograms of $Ru_xIr_{(1-x)}O_2/C$ were recorded at scan rates between 1 and 500 mV s^{-1} from 0.05 V to 1.4 V vs. RHE. Figs. 6a and b present as examples the CVs obtained for RuO_2/C and IrO_2/C materials, respectively. When increasing the scan rate, the current densities increase while the CV shape remains the same. The redox transitions described and attributed previously are accompanied by proton transfer, which is a faradaic process occurring only on the material surface. The formation of hydroxide surface species follows Eq. (1) [32].

$$MO_x(OH)_y + \delta H^+ + \delta e^- = MO_{x-\delta}(OH)_{y+\delta} \qquad (1)$$
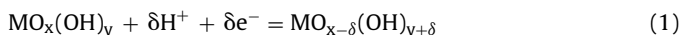
where M is the metal species, Ru or Ir. In the studied potential range, the current densities recorded correspond to the sum of two contributions. The first one is the formation of the surface hydroxides and the second one is a capacitive contribution resulting of charge accumulation at the electrode/electrolyte interface. Because the recorded current densities are due to electrode/electrolyte interface processes, the capacitances of $Ru_xIr_{(1-x)}O_2/C$ materials were determined by calculating the average charge and discharge current density values. The specific capacitances (C in F g^{-1}) were obtained using Eq. (2) by integration of the CV curves at different scan rates:

$$C = \frac{1}{v \times m \times (E_2 - E_1)} \int_{E_1}^{E_2} j(E)dE \qquad (2)$$

where v is the scan rate (V s^{-1}), m is the mass in mg of oxide species in the $Ru_xIr_{(1-x)}O_2/C$ material deposited on the working electrode, E_1 and E_2 are the lower and upper potential limits for the integration curves (0.2 and 1.2 V vs. RHE, respectively) and $j(E)$ the current density at electrode potential E.

Fig. 6c shows the changes of the specific capacitance for $Ru_xIr_{(1-x)}O_2/C$ materials as a function of the scan rate. All capac-
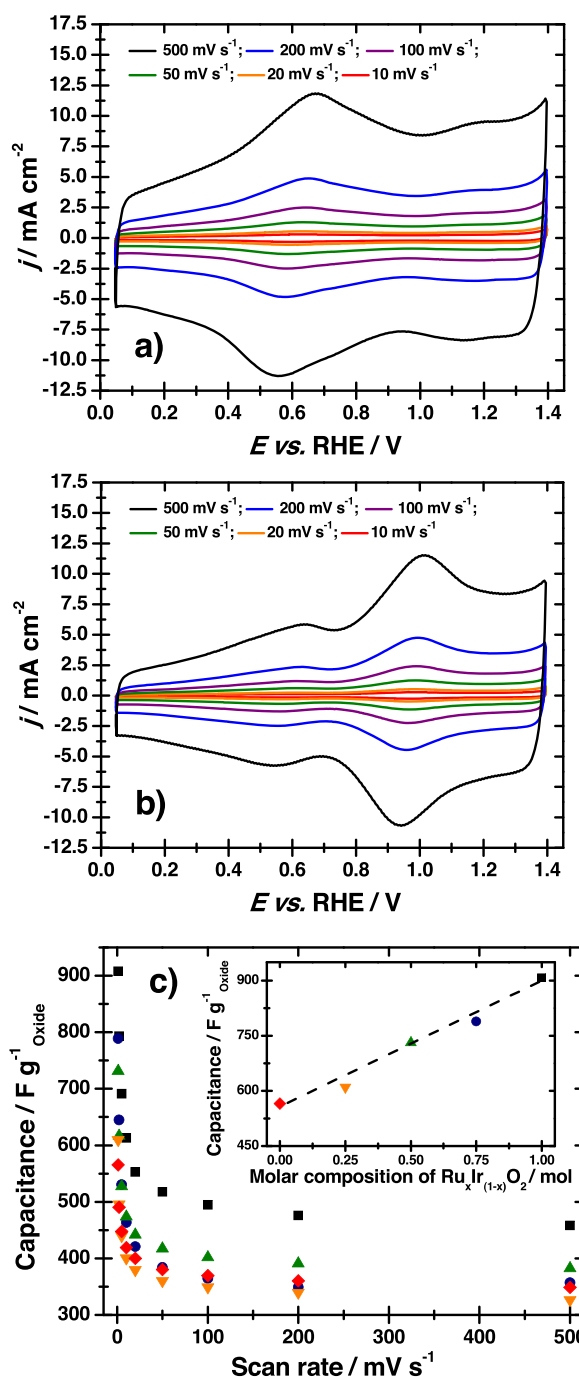

Fig. 6. Cyclic voltammograms of (a) RuO_2/C and (b) IrO_2/C based electrodes recorded in 0.5 M H_2SO_4 electrolyte at different scan rates; (c) Change of the specific capacitances normalized by the metal oxide mass, measured at different scan rates for $Ru_xIr_{(1-x)}O_2/C$ (■ RuO_2, ● $Ru_{0.75}Ir_{0.25}O_2$, ▲ $Ru_{0.5}Ir_{0.5}O_2$, ▼ $Ru_{0.25}Ir_{0.75}O_2$ and ◆ IrO_2). Inset: capacitance values obtained at 1 mV s^{-1} as a function of the molar composition of the ruthenium-iridium mixed oxides.

itances reach values higher than 300 F g $_{Oxides}$ $^{-1}$, which reveals the high capacitive properties of the materials. However, the capacitance values decrease drastically for scan rate between 1 mV s^{-1} and 50 mV s^{-1}. For higher scan rates, the capacitance values stabilize. This behavior is linked to the diffusion of electro-reactive species from the bulk electrolyte to adsorption active sites in the catalytic layer. At high scan rates, the adsorption of electro-reactive species only occurs at the most accessible surface electroactive sites, whereas at low scan rates the adsorption takes place on active sites in the bulk of the whole material. Although higher capaci-
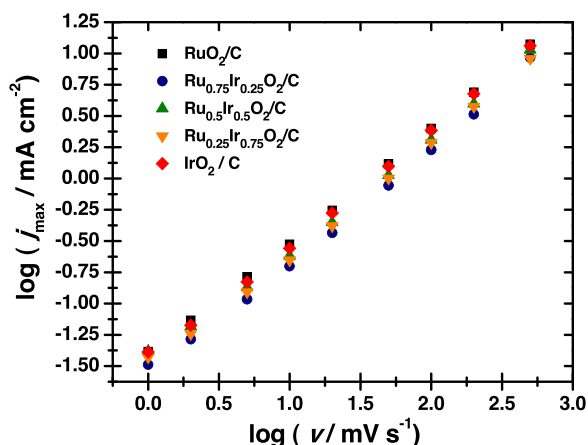
Fig. 7. Graphs of log (j_{max}) as a function of log (v) obtained for $Ru_xIr_{(1-x)}O_2$/C based electrodes in 0.5 mol L^{-1} H_2SO_4 electrolyte.

tance values are obtained for ruthenium oxides, the iridium oxide modified catalysts display capacitance values of the same order.

Inset in Fig. 6c shows the capacitance values measured at 1 mV s^{-1} as a function of the mixed-oxides composition. An increasing linear relationship with the Ru atomic ratio is obtained. Since the mean particles sizes remain constant for all $Ru_xIr_{(1-x)}O_2$/C materials, the capacitive properties seem to be higher for ruthenium oxide than for iridium oxide.

When increasing the scan rate, slight shifts of the apparent peaks on the CV are observed at higher potentials for the anodic sweep and at lower potentials for the cathodic sweep. This phenomenon could come from a non-reversibility of the reactions occurring at the electrolyte/electrode interface. The accumulation of charges can be limited by the diffusion of electro-reactive species towards the active sites or by their adsorption on active sites. To determine the rate determining step which controls the charge transfer occurring at the electrolyte/material interface log (j_{max}) was plotted as a function of log (v) (Fig. 7). Because of their higher intensity, the redox peak corresponding to Ru(III)/Ru(IV) is considered for RuO_2/C and for $Ru_{0.75}Ir_{0.25}O_2$/C electrocatalysts, whereas that of Ir(IV)/Ir(VI) is considered for the Ir-rich catalysts. Linear plots are obtained, from which the slopes were determined (Table 2). All the slope values are close to 1 which indicates that the reaction at the electrolyte/material interface is limited by adsorption of the electroreactive species.

The voltammetric charges (q^*) are considered to be proportional to the active surface area or to the number of active sites in the catalytic layer and can be determined from the CVs [33]. The anodic and cathodic charges are calculated from the integration of the voltammograms between 0.2 and 1.2 V vs RHE. The ratios of the anodic charge to the cathodic charge are close to 1 for each scan rate, thus the reactions are reversible. The charge q^* is determined by averaging of the cathodic and anodic charge values. But, as discussed previously, the reaction occurs on all active sites at very low scan rate (1 mV s^{-1}) because the electro-reactive species can diffuse inside the porosity of the catalytic layer, whereas at higher scan rates the reaction can only take place on the most accessible active sites. Ardizzone et al. [34] established the Eqs. (3) and (4) based on the diffusion of electro-reactive species at the electrode/electrolyte interface in order to determine the total charges (q^*_{Total}) and the most accessible charges (q^*_{Outer}) when the scan rates values tend to 0 and +∞, respectively.

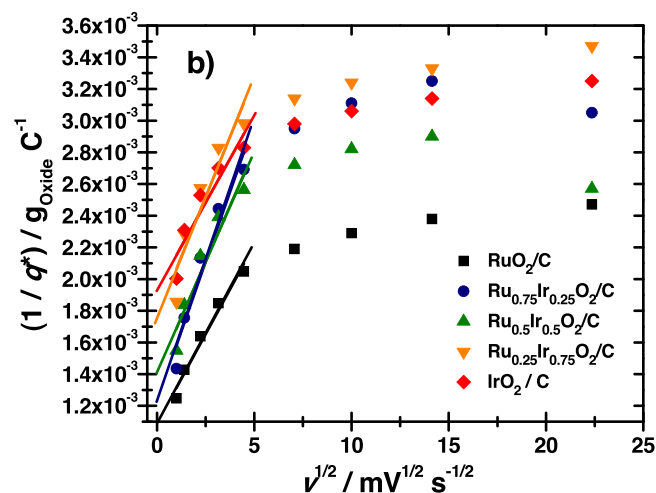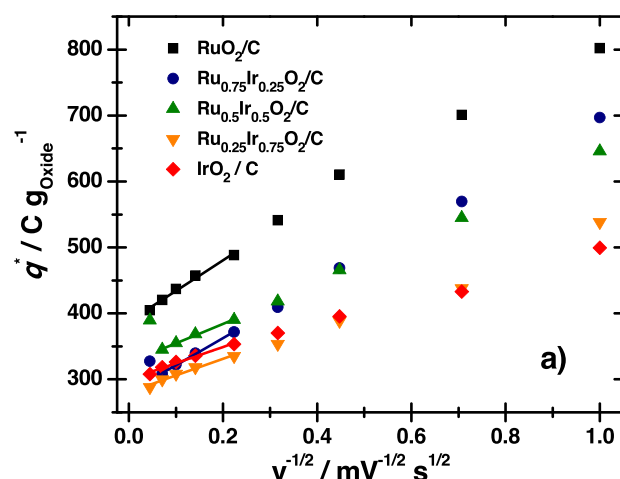$$\frac{1}{q^*} = \frac{1}{q^*_{Total}} + C_2\sqrt{v} \tag{3}$$

Fig. 8. Dependence of the voltammetric charges with scan rate: (a) extrapolation of the most accessible charges (q^*_{outer}) and (b) extrapolation of the total charges (q^*_{total}).

$$q^* = q^*_{Outer} + C_1\frac{1}{\sqrt{v}} \tag{4}$$

where C_1 and C_2 are constants, v is the scan rate and q^* are the average charges calculated for each scan rate v. The q^*_{Outer} values are obtained by determining the intercepts of the linear part of the curves for scan rate values higher than 20 mV s^{-1} (Fig. 8a), whereas the q^*_{Total} values are obtained for scan rate values lower than 20 mV s^{-1} (Fig. 8b). Fig. 9 plots the q^*_{Outer} and q^*_{Total} values as a function of the mixed-oxide composition; the values obtained are summarized in Table 2. The q^*_{Total} obtained for RuO_2/C are higher than those obtained for IrO_2/C (917.4 and 518.1C g_{Oxide}^{-1} respectively), and mixed oxides led to intermediate values. A decreasing linear relationship with the Ir ratio is obtained. Considering the most accessible active sites, q^*_{Outer}, the changes in q^*_{Outer} with the Ru content is less pronounced but the value increases from 299.7 to 387.7C g^{-1}_{Oxide} for IrO_2/C and RuO_2/C respectively.

The active sites accessibility, q^*_{Outer}/q^*_{Total}, was then determined (Fig. 9b). The highest active sites accessibility was found for the IrO_2/C material, representing 58% of the active sites, whereas for pure ruthenium oxide the value falls down to 42%. Accessibility values of the mixed oxides are intermediate, following a linear relationship. This observation allows assuming that the well-dispersed mixed metal oxide particles on the carbon support and their small sizes lead to a linear combination of the properties of IrO_2 and RuO_2 without synergistic effect. Since the mean particle sizes are iden-

Table 2
Electrochemical data obtained for $Ru_xIr_{(1-x)}O_2/C$ materials synthesized by the modified polyol synthesis method (S = slope of the $Log(j_{max}) = f(log(v))$ plots, q^*_{total} = total voltammetric charge, q^*_{outer} = most accessible charge, A = accessibility and b = Tafel slope).

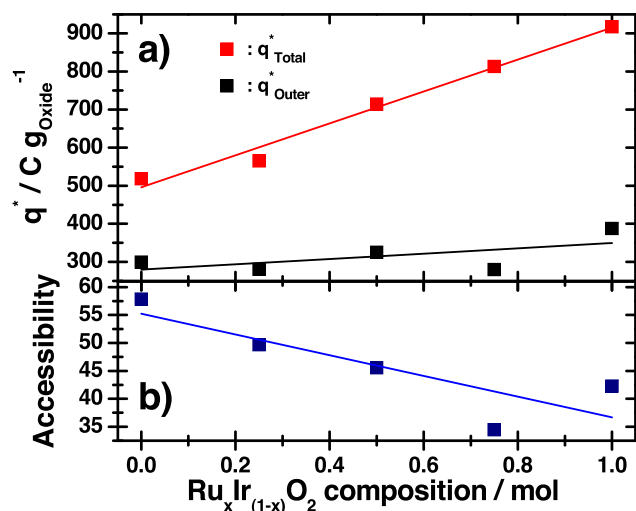|	$Log(j_{max}) = f(log(v))$	$q^*_{total}/C\ g_{oxide}{}^{-1}$	$q^*_{outer}/C\ g_{oxide}{}^{-1}$	Aq^*_{outer}/q^*_{total}	$b/mV\ dec^{-1}$
RuO_2/C	0.91	917.4	387.7	42.2	49.1
$Ru_{0.75}Ir_{0.25}O_2/C$	0.91	813.0	280.0	34.4	53.8
$Ru_{0.5}Ir_{0.5}O_2/C$	0.89	714.2	325.2	45.5	54.8
$Ru_{0.25}Ir_{0.75}O_2/C$	0.90	564.9	280.7	49.7	61.4
IrO_2/C	0.92	518.1	299.7	57.8	70.4

Fig. 9. (a) Total charges (q^*_{total}) and most accessible charges (q^*_{outer}) and (b) active site accessibility (q^*_{outer}/q^*_{total}) as a function of the Ru content in $Ru_xIr_{(1-x)}O_2/C$.
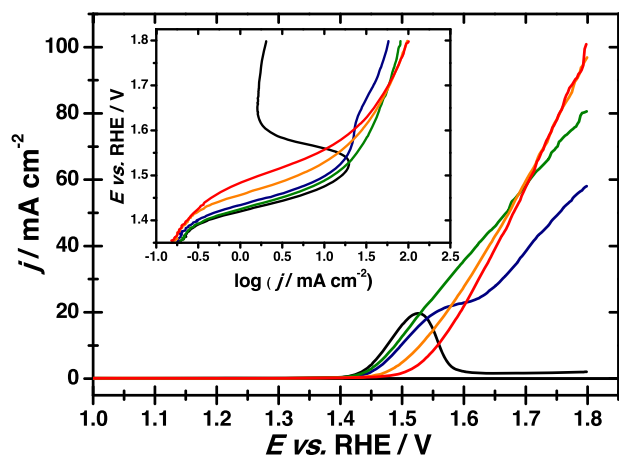
Fig. 10. Polarization curves of $Ru_xIr_{(1-x)}O_2/C$ with x = 1 (black line), x = 0.75 (blue line), x = 0.5 (red line), x = 0.25 (green line) and x = 0 (orange line), recorded in 0.5 M H_2SO_4 at 5 mV s^{-1} and T = 20 °C. Inset: corresponding Tafel plot for the OER. (For interpretation of the references to colour in this figure legend, the reader is referred to the web version of this article.)

tical in all samples and the active sites accessibility is the lowest for RuO_2/C, the capacitance results can clearly be attributed to the inherent capacitive properties of the ruthenium oxide.

To evaluate the electrocatalytic properties toward the oxygen evolution reaction (OER) of the mixed metal oxide catalysts, polarization curves were recorded from 0.8 to 1.8 V vs. RHE at 5 mV s^{-1}, in order to avoid, as much as possible, the support oxidation (Fig. 10). The currents were normalized by the geometric surface area of the working electrode in order to compare the performances for a same mixed metal oxide loading. All catalysts led to abundant bubbling

of oxygen on the electrode surface, but the shape of the polarization curves is different depending on the material composition.

In the case of the pure RuO_2/C material, the current density starts to increase from ca. 1.40 V vs. RHE, reaches a maximum values at 1.525 V vs. RHE and then decreases drastically down to ca. 1.7 mA cm^{-2}. Similar behaviors were already reported for hydrous or non-crystalline ruthenium oxides [11,35] although the involved reactions and mechanisms are not clearly defined. Nevertheless, the anodic current from 1.4 to 1.525 V vs. RHE is attributed to the water oxidation, since bubbling was observed at the electrode surface. The passivation of the electrode material for higher potentials is not clearly understood but could come from oxide material instabilities induced by the hydration, the size and the low crystallinity of the ruthenium oxide particles. The residual current at high overpotentials certainly comes from the carbon support oxidation. This observation confirms that the contribution of the support oxidation in the whole current recorded is negligible.

In the case of the pure IrO_2/C material, the OER starts at a potential higher than that for pure ruthenium oxide (at ca. 1.475 V vs. RHE, close to 1.48 V, i.e. at the thermo-neutral voltage), as it has been often described in the literature [36,37]. From ca. 1.40 V vs. RHE to ca. 1.55 V vs. RHE, the RuO_2 material leads to higher efficiency for OER than the IrO_2 material. For higher potentials, the passivation of the IrO_2/C catalyst does not occur, and the current density increases monotonously. The high electrocatalytic efficiency of the IrO_2 particles for the water splitting reaction may come from the higher crystallinity of the particles and from the absence of chemically adsorbed water in the oxide lattice, conversely to the RuO_2 material, as observed through Raman and TGA analyses.

In the case of mixed oxide materials, when increasing the ruthenium molar ratio, the OER onset potential decreases down to a value close to that for pure ruthenium oxide catalyst. At low overpotentials, the electrocatalytic efficiency for the OER is higher than that of IrO_2/C, whereas for high overpotentials this trend is reversed. This behavior at high potentials can be related to the decrease of the active site number in the catalytic layer, owing to the passivation of the particles by the hydrous and/or non-crystalline ruthenium oxide phases. Especially considering the $Ru_{0.75}Ir_{0.25}O_2/C$ material, the shoulder appearing in the polarization curves at ca. 1.57 V vs. RHE confirms the occurrence of the passivation process. Nevertheless due to the presence of the IrO_2 sites, activity of mixed oxide catalysts towards the OER remains at higher overpotentials.

Looking at the polarization curves in Fig. 10, it can be proposed that in an electrolysis cell, the most efficient catalyst composition is depending on the cell working point (considering that the hydrogen evolution reaction is not limiting the electrolysis process and that the cathode potential remains close to 0 V): pure RuO_2 nanoparticles present the best activity for $U_{cell} < 1.5$ V, mixed $Ru_{0.5}Ir_{0.5}O_2$ nanoparticles present the best activity for 1.5 V < U_{cell} < 1.65 V and pure IrO_2 nanoparticles present the best activity for U_{cell} > 1.65 V. In order to discard the different metal oxide composition, further works will be performed with catalytic metal oxide nanoparticles deposited on a stable support suitable for electrolysis cell working conditions to determine the cell voltage at 1 A cm^{-2}.

The Tafel plots are given in the inset of Fig. 10. At low overpotentials, it can be assumed that ohmic drop has no effect on the j-E measurements [38,39], so that the Tafel slopes were measured in the potential range from 1.4 and 1.55 V vs. RHE, where $j < 20$ mA cm^{-2}. The values were determined by fitting the most linear part of the curves and are summarized in Table 2. Due to the complex reaction involving a 4-electrons transfer for water oxidation, several mechanisms were considered with different rate-determining steps [40], starting from the water adsorption on the active site (S) with a charge transfer leading to intermediate hydroxyl species:

$$S + H_2O \rightarrow S-OH_{ads} + H^+ + e^- \,(R1)$$

the second step is the deprotonation of the intermediate species leading to a second intermediate specie:

$$S-OH_{ads} \rightarrow S-O_{ads} + H^+ + e^- \,(R2)$$
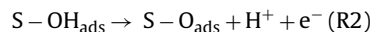
finally, the combination of two intermediate species leads to the formation of O_2:

$$S-O_{ads} \rightarrow 2S + O_2 \,(R3)$$
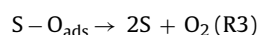
It has been shown elsewhere that the Tafel slope values should be 120 mV dec^{-1}, 40 mV dec^{-1} and 15 mV dec^{-1} for (R1), (R2) and (R3) being the rate determining steps (rds), respectively [41]. However, other authors [41–43] explained that, due to the catalytic layer composition, the bond strength of intermediate species to the active sites could differ and thus could lead to different Tafel slope values. Actually, they dissociated the (R1) step in two reactions:

$$S + H_2O \rightarrow S-OH^*_{ads} + H^+ + e^- \,(R1')$$
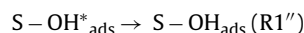
$$S-OH^*_{ads} \rightarrow S-OH_{ads} \,(R1'')$$

where, the intermediate species $S-OH_{ads}$ and $S-OH^*_{ads}$ have the same chemical structure but different bond strengths according to the active site nature. Both steps can occur alternatively or in parallel, and the Tafel slope value is then 60 mV dec^{-1}.

In addition, depending on the bond strength of the intermediate species, a chemical reaction can take place in parallel to the step (R2):

$$2S-OH_{ads} \rightarrow S-O_{ads} + S + H_2O \,(R2')$$

leading to a Tafel slope value of 30 mV dec^{-1}. The Tafel slope value for the Ru$_x$Ir$_{(1-x)}$O$_2$/C catalysts (Table 2) decreases when increasing the ruthenium atomic content, suggesting improvement of the efficiency and of the kinetic parameters for the water oxidation reaction. For RuO$_2$/C and IrO$_2$/C, the Tafel slope values are 49.1 and 70.4 mV dec^{-1}, respectively, and are in agreement with those given in other works [28,36], although slightly higher (40 and 60 mV dec^{-1} for RuO$_2$ and IrO$_2$, respectively). This small discrepancy can be due to the low weight loading of the metal oxide in the electrode and to the carbon oxidation occurring simultaneously with the water oxidation reaction. Anyway, taking into account the established mechanism, it can be proposed that (R2) is the rds for catalysts with ruthenium atomic ratios higher than 0.5, whereas combination of (R1') and (R1") is the rds for the Ir rich catalysts.

6. Conclusion

It was first shown the possibility to synthesize dispersed nanostructured Ru$_x$Ir$_{(1-x)}$O$_2$ metal oxides with controlled sizes (from 1 to 3 nm) and compositions, displaying supercapacitive and catalytic properties. Moreover, the following general highlights can be pointed out:

(1) The properties can be tuned by the control of the mixed oxide composition.
(2) Pure RuO$_2$ present the highest supercapacitive properties, but the addition of iridium leads to decrease this property.
(3) Pure RuO$_2$ presents the lower onset potential for OER, but tends to passivate at higher potentials.
(4) Addition of iridium leads to limit or avoid the catalyst passivation and to increase the activity at high potentials, but also to increase the OER onset potential.
(5) Pure RuO$_2$ nanoparticles present the best activity for $U_{cell} < 1.5$ V, mixed Ru$_{50}$Ir$_{50}$O$_2$ nanoparticles present the best activity for 1.5 V $< U_{cell} < 1.65$ V and pure IrO$_2$ nanoparticles present the best activity for $U_{cell} > 1.65$ V.
(6) The mechanism of the OER at the mixed oxide catalysts was determined from the analysis of the Tafel slopes, and it was shown that this mechanism was dependent on the Ru/Ir ratio.

References

[1] S.K. Mazloomi, N. Sulaima, Influencing factors of water electrolysis electrical efficiency, Renewable Sustainable Energy Rev. 16 (2012) 4257–4263.
[2] M. Balat, Potential importance of hydrogen as a future solution to environmental and transportation problems, Int. J. Hydrogen Energy 33 (2008) 4013–4029.
[3] C. Coutanceau, S. Baranton, Electrochemical conversion of alcohols for hydrogen production: a short overview, WIREs Energy Environ. (2016), http://dx.doi.org/10.1002/wene.193.
[4] J.P. Zheng, P.J. Cygan, T.R. Jow, Hydrous ruthenium oxide as an electrode material for electrochemical capacitors, J. Electrochem. Soc. 142 (1995) 2699–2703.
[5] T. Liu, W.G. Pell, B.E. Conway, Self-discharge and potential recovery phenomena at thermally and electrochemically prepared RuO$_2$ supercapacitor electrodes, Electrochim. Acta 42 (1997) 3541–3552.
[6] S. Trasatti, Electrocatalysis: understanding the success of DSA®, Electrochim. Acta 36 (1991) 225–241.
[7] S. Trasatti, G. Lodi, Oxygen and chlorine evolution at conductive metallic oxide anodes, in: S. Trasatti (Ed.), Electrodes of Conductive Metallic Oxides, vol. B, Elsevier, Amsterdam, 1981, pp. 521–626.
[8] M. Carmo, D.L. Fritz, J. Mergel, D. Stolten, A comprehensive review on PEM water electrolysis, Int. J. Hydrogen Energy 38 (2013) 4901–4934 (and reference therein).
[9] T. Audichon, E. Mayousse, S. Morisset, C. Morais, C. Comminges, T.W. Napporn, K.B. Kokoh, Electroactivity of RuO$_2$-IrO$_2$ mixed nanocatalysts toward the oxygen evolution reaction in a water electrolyzer supplied by a solar profile, Int. J. Hydrogen Energy 39 (2014) 16785–16796.
[10] R.R.L. Pelegrino, L.C. Vicentin, A.R. De Andrade, R. Betazzoli, Thirty minutes laser calcination method for the preparation of DSA® type oxide electrodes, Electrochem. Commun. 4 (2002) 139–142.
[11] A. Devadas, S. Baranton, T.W. Napporn, C. Coutanceau, Tailoring of RuO$_2$ nanoparticles by microwave assisted Instant method for energy storage applications, J. Power Sources 196 (2011) 4044–4053.
[12] J.-Y. Kim, K.-H. Kim, S.-H. Park, K.-B. Kim, Microwave-polyol synthesis of nanocrystalline ruthenium oxide nanoparticles on carbon nanotubes for electrochemical capacitors, Electrochim. Acta 55 (2010) 8056–8061.
[13] Z.-S. Wu, D.-W. Wang, W. Ren, J. Zhao, G. Zhou, F. Li, H.-M. Cheng, Anchoring hydrous RuO$_2$ on graphene sheets for high-performance electrochemical capacitors, Adv. Funct. Mat. 20 (2010) 3595–3602.
[14] H. Kim, B.N. Popov, Characterization of hydrous ruthenium oxide/carbon nanocomposite supercapacitors prepared by a colloidal method, J. Power Sources 104 (2002) 52–61.
[15] Y.-T. Shih, K.-Y. Lee, Y.-S. Huang, Characterization of iridium dioxide?carbon nanotube nanocomposites grown onto graphene for supercapacitor, J. Alloys Compd. 619 (2015) 131–137.
[16] P.C. Liao, Y.S. Huang, K.K. Tiong, Characterization of RuO$_2$ and IrO$_2$ films deposited on Si substrate, J. Alloys Compd. 317–318 (2001) 98–102.
[17] A.V. Korotcov, Y.S. Huang, D.S. Tsai, K.K. Tiong, Raman scattering characterization of vertical aligned 1D IrO$_2$ nanocrystals grown on single crystal oxide substrates, Solid State Commun. 137 (2006) 310–314.

[18] E. Tsuji, A. Imanishi, K.-I. Fukui, Y. Nakato, Electrocatalytic activity of amorphous RuO_2 electrode for oxygen evolution in an aqueous solution, Electrochim. Acta 56 (2011) 2009–2016.

[19] J.-Y. Kim, K.-H. Kim, H.-K. Kim, S.-H. Park, K.C. Roh, K.-B. Kim, Template-free synthesis of ruthenium oxide nanotubes for high-performance electrochemical capacitors, ACS Appl. Mater. Interfaces 7 (2015) 16686–16693.

[20] Y.S. Huang, F.H. Pollak, Raman investigation of rutile RuO_2, Solid State Comm. 43 (1982) 921–924.

[21] R.S. Chen, C.C. Chen, Y.S. Huang, C.T. Chia, H.P. Chen, D.S. Tsai, K.K. Tiong, A comparative study of microstructure of RuO_2 nanorods via Raman scattering and field emission scanning electron microscopy, Solid State Comm. 131 (2004) 349–353.

[22] D. Rochefort, P. Dabo, D. Guay, P.M.A. Sherwood, XPS investigations of thermally prepared RuO_2 electrodes in reductive conditions, Electrochim. Acta 48 (2003) 4245–4252.

[23] R.-S. Chen, Y.-S. Huang, Y.-M. Liang, D.-S. Tsai, Y. Chi, J.-J. Kai, Growth control and characterization of vertically aligned IrO_2 nanorods, J. Mater. Chem. 13 (2003) 2525–2529.

[24] L.-Â. Näslund, Á.S. Ingason, S. Holmin, J. Rosen, Formation of $RuO(OH)_2$ on RuO_2-based electrodes for hydrogen production, J. Physical Chem. C 118 (2014) 15315–15323.

[25] M. Schaefer, R. Schlaf, Electronic structure investigation of atomic layer deposition ruthenium(oxide) thin films using photoemission spectroscopy, J. Appl. Phys. 118 (2015) 065306-1–065306-7.

[26] J. Cheng, H. Zhang, H. Ma, H. Zhong, Y. Zou, Study of carbon-supported IrO_2 and RuO_2 for use in the hydrogen evolution reaction in a solid polymer electrolyzer, Electrochim. Acta 55 (2010) 1855–1861.

[27] K.-H. Chang, C.-C. Hu, C.-Y. Chou, Textural and capacitive characteristics of hydrothermally derived $RuO_2 \cdot xH_2O$ nanocrystallites: independent control of crystal size and water content, Chem. Mater. 19 (2007) 2112–2119.

[28] F.I. Mattos-Costa, P. de Lima-Neto, S.A.S. Machado, L.A. Avaca, Characterisation of surfaces modified by sol-gel derived $Ru_xIr_{1-x}O_2$ coatings for oxygen evolution in acid medium, Electrochim. Acta 44 (1998) 1515–1523.

[29] K. Juodkazis, J. Juodkazytė, V. Šukienė, A. Grigucevičienė, A. Selskis, On the charge storage mechanism at $RuO_2/0\,5\,M\,H_2SO_4$ interface, J. Solid State Electrochem. 12 (2008) 1399–1404.

[30] J. Ribeiro, M.S. Moats, A.R. De Andrade, Morphological and electrochemical investigation of $RuO_2–Ta_2O_5$ oxide films prepared by the Pechini–Adams method, J. Appl. Electrochem. 38 (2008) 767–775.

[31] D. Galizzioli, F. Tantardini, S. Trasatti, Ruthenium dioxide: a new electrode material: i. Behaviour in acid solutions of inert electrolytes, J. Appl. Electrochem. 4 (1974) 57–67.

[32] C.-C. Hu, K.-H. Chang, Cyclic voltammetric deposition of hydrous ruthenium oxide for electrochemical capacitors: effects of codepositing iridium oxide, Electrochim. Acta 45 (2000) 2685–2696.

[33] S. Ardizzone, S. Trasatti, Interfacial properties of oxides with technological impact in electrochemistry, Adv. Coll. Interface Sci. 64 (1996) 173–251.

[34] S. Ardizzone, G. Fregonara, S. Trasatti, Inner and Outer active surface of RuO_2 electrodes, Electrochim. Acta 35 (1990) 263–267.

[35] T. Audichon, T.W. Napporn, C. Canaff, C. Morais, C. Comminges, K.B. Kokoh, IrO_2 coated on RuO_2 as efficient and stable electroactive nanocatalysts for electrochemical water splitting, J. Phys. Chem. C 120 (2016) 2562–2573.

[36] R. Kötz, S. Stucki, Stabilisation of RuO_2 by IrO_2 for anodic oxygen evolution in acid media, Electrochim. Acta 31 (1986) 1311–1316.

[37] J. Cheng, H. Zhang, G. Chen, Y. Zhang, Study of $Ir_xRu_{1-x}O_2$ oxides as anodic electrocatalysts for solid polymer electrolyte water electrolysis, Electrochim. Acta 54 (2009) 6250–6256.

[38] L.-E. Owe, M. Tsypkin, K.S. Wallwork, R.G. Haverkamp, S. Sunde, Iridium?ruthenium single phase mixed oxides for oxygen evolution: composition dependence of electrocatalytic activity, Electrochim. Acta 70 (2012) 158–164.

[39] M.H.P. Santana, L.A. De Faria, Oxygen and chlorine evolution on $RuO_2 + TiO_2 + CeO_2 + Nb_2O_5$ mixed oxide electrodes, Electrochim. Acta 51 (2006) 3578–3585.

[40] Y. Matsumoto, E. Sato, Electrocatalytic properties of transition metal oxides for oxygen evolution reaction, Mater. Chem. Phys. 14 (1986) 397–426.

[41] L.A. De Faria, J.F.C. Boodts, S. Trasatti, Electrocatalytic properties of ternary oxide mixtures of composition $Ru0\,3Ti_{(0.7-x)}Ce_xO_2$: oxygen evolution from acidic solution, J. Appl. Electrochem. 26 (1996) 1195–1199.

[42] E. Antolini, Iridium as catalyst and cocatalyst for oxygen Evolution/Reduction in acidic polymer electrolyte membrane electrolyzers and fuel cells, ACS Catal. 4 (2014) 1426–1440.

[43] L.M. Da Silva, J.F.C. Boodts, L.A. De Faria, Oxygen evolution at $RuO_{2(x)} + Co_3O_{4(1-x)}$ electrodes from acid solution, Electrochim. Acta 46 (2001) 1369–1375.